CRYSTAL GROWTH & DESIGN

Article

pubs.acs.org/crystal

Nanocystals of Hematite with Unconventional Shape-Truncated Hexagonal Bipyramid and Its Optical and Magnetic Properties

Thanh-Khue Van,[†] Hyun Gil Cha,[†] Cuong Ky Nguyen,[†] Soo-Whan Kim,[‡] Myun-Hwa Jung,[‡] and Young Soo Kang*[,†]

[†]Korea Center for Artificial Photosynthesis and Department of Chemistry, Sogang University, Shinsu-dong #1, Mapo-gu, Seoul 121-854, Korea

[‡]Department of Physics, Sogang University, Seoul 121-742, Korea

ABSTRACT: The capping agent plays a critical function in anisotropic crystal growth to induce polyhedral morphology of a nanocrystal. Uniform and single-crystalline α-Fe_2O_3 polyhedral nanoparticles in the hexagonal single crystal system named truncated hexagonal bipyramid for the first time were successfully synthesized by a facile one-step hydrothermal method with the aid of carboxymethyl cellulose and hydrazine molecules. The appearance and crystal structure of these iron oxide nanoparticles were characterized in detail by physicochemical methods. The results show that the as-synthesized α-Fe_2O_3 particles are bound by 12 same-side crystalline facets {101} and two other same facets {001} at the tops. These obtained iron oxide particles belong to a pure hematite phase, and the particle size is around 400 nm. The optical property of the as-synthesized product was analyzed, and the determined indirect band gap value E_g is 2.08 eV. The magnetic property studies of truncated hexagonal bipyramid hematite particles have shown that this kind of α-Fe_2O_3 possess a weak ferromagnetism under the T_M, and the saturation points do not reach up to the maximum applied magnetic field. Role of the reactants was discussed and investigated systematically in the work. Furthermore, a schematic illustration for the probable formation of this α-Fe_2O_3 morphology in whole of the synthetic process was also proposed.

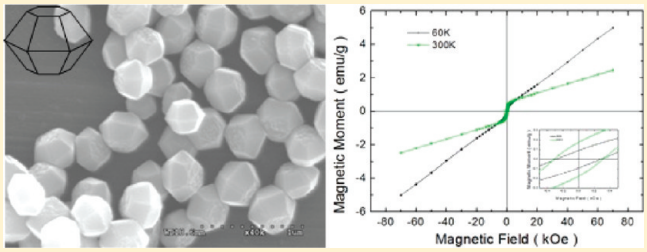

INTRODUCTION

Many nanomaterials are in different stages of research and development. Each type possesses specific properties that are potentially applicable to solve the problem of insufficient energy in the world. The physical and chemical properties of the nanomaterials are dependent not only on their components but also strongly on their size and morphology because the proportion of the surface atom is determined by size of the particles, and the crystalline structure of the particle surface depends on the particle shape.[1] Among metal oxide nanomaterials, hematite (α-Fe_2O_3), an n-type semiconductor, has attracted great attention from researchers[2−6] because of its optimal optical band gap (E_g = 2.1 eV, which is capable of absorbing light up to 600 nm),[7] thermodynamic stability in oxidative environment, nontoxicity, abundance, and low processing cost. However, challenges are set by its poor conductivity, a short hole-diffusion length, L_D, of only 2−4 nm,[8] and very short excited-state lifetime of ~10^{-26} s[9] that have to be overcome before this material can be used for practical applications. Therefore, the fabrication of size- and shape-controlled nanostructures is very important for the control of their physicochemical properties that hold promise for the design of novel materials, devices, and techniques with various applications in sensors, catalysts, information storage, biotechnology, water splitting, etc.[5,10−13] In recent years, hematite material was synthesized through various strategies. For instance, Wang and co-workers[14] applied a simple impregnating method to prepare hollow spheres of Fe_2TiO_5/α-Fe_2O_3 nanocomposite, which showed much improved gas-sensing properties for some organic gases. By adjusting the polarity of the mixed solvent, Yu et al.[15] could controllably fabricate various morphologies of α-Fe_2O_3, which critically affected the magnetic properties. In another example, Wang and co-workers[16] have synthesized uniform α-Fe_2O_3 nanorods on a large scale by a simple and direct 1,2-propanediamine-assisted hydrothermal method. The role of the reaction parameters and magnetic properties of the product in this work were examined systematically as well. Up to now, although many approaches for the preparation of hematite in various morphologies such as hierarchical mesoporous hematite microspheres,[17] acicular α-Fe_2O_3 nanoparticles,[18] hematite nanocubes,[19] iron oxide tubes in tube nanostructures,[20] hollow spheres,[21] cigar-shaped ferrite nanocrystals, dendritic, urchinlike α-Fe_2O_3 nanorings,[22−25] etc. have been reported, it is still a big challenge to produce them in large homogeneous quantities in polyhedral single-crystalline nanoparticle forms because the surface energy of several low-index planes of crystalline structure are quite similar and strongly depend on synthesis parameters.[26−28]

Received: September 23, 2011
Revised: November 30, 2011
Published: January 3, 2012

In the present contributions, homogeneous polyhedral single-crystalline α-Fe_2O_3 nanoparticles in the hexagonal crystalline system named truncated hexagonal bipyramid (THB) were synthesized for the first time through a facile one-step hydrothermal method with the aid of carboxymethyl cellulose sodium salt (CMC) and hydrazine (N_2H_4) molecules. The crucial roles of CMC and N_2H_4 molecules used in this route are as dispersant agents and capping agents, respectively, to control the uniformity, size, and shape of the particles. The obtained THB particle product is enclosed by 12 symmetric side trapezoidal facets {101} and two hexagonal facets {001} at two tops. The particle size was determined as around 400 nm. The optical property of this kind was also investigated. Magnetic behavior of this hematite morphology revealed that THB α-Fe_2O_3 possesses a weak ferromagnetism under the Morin transition temperature, T_M, and the saturation points do not reach up to the maximum applied magnetic field. The influence of reactants during the whole of the synthetic process on the morphology of the α-Fe_2O_3 particles resulting in various morphologies was also systematically investigated. In addition, a possible mechanism and crystal growth processes to create these morphologies was proposed schematically.

EXPERIMENTAL SECTION

Materials and Reagents. Potassium hexacyanoferrate(III) ($K_3[Fe(CN)_6]$), sodium carboxymethyl cellulose (CMC, M_w = 250 000), hydrazine hydrate solution ($N_2H_4{\cdot}xH_2O$, 60%) was purchased from Aldrich. All the reagents were AR grade and used in the synthetic process without further purification. Distilled deionized water (DDW) was used throughout the experiment.

Synthesis. In our experiment, the truncated hexagonal bipyramid α-Fe_2O_3 nanoparticles were synthesized by a hydrothermal method. In a typical synthetic procedure, a mixture of 20 mL solution of $K_3[Fe(CN)_6]$ (0.02 M), CMC (3.5 g L^{-1}), and N_2H_4 (1.5%) was stirred for a few moments before being transferred into a Teflon-lined (poly(tetrafluoroethylene)-lined) stainless steel autoclave. The hydrothermal treatment process was carried out at 160 °C and maintained for 8 h. After the hydrothermal treatment, the reaction was cooled under cool water at the room temperature. The dark red precipitated product was isolated by centrifugation, repeatedly washed with absolute ethanol and distilled water, and dried at 80 °C in air. When the concentration of N_2H_4 was changed to 4.5%, 6.0%, and 8.0% while the other reagents were kept in constant, octahedral, oblique cubic, and shape-unidentified morphologies were obtained, respectively, by the same procedure.

For the dendritic morphology, 20 mL solution of $K_3[Fe(CN)_6]$ (0.02 M) was kept at 160 °C under hydrothermal conditions for 8 h and cooled to room temperature naturally. Finally, the produced hematite dendritic product was separated by centrifugation, washed with a copious absolute ethanol and water, and dried at 80 °C in the air. A similar procedure was used with the addition of CMC (3.5 g L^{-1}) in the reaction solution. The final hematite product is a spherical morphology.

Characterization Techniques. The crystal structure of the material was examined with X-ray diffraction on a Rigaku miniFlex-II desktop X-ray diffractometer, Cu Kα radiation with λ = 0.154056 nm. The diffraction patterns were recorded from 20° to 80° 2θ range with step size of 0.02° at 2°/min. UV–vis spectra of THB α-Fe_2O_3 powder were taken with a Shimadu UV-310PC. Magnetic measurements for the samples in the powder form were carried out with a Quantum Design MPMS SQUID VSM DC magnetometer. Scanning electron microscopy (SEM) (Hitachi S-4300 FE-SEM) and JEOL transmission electron microscopy (TEM) with JEM 2100F installed with EDX operated at accelerating at 200 keV was used for analysis of morphology and crystal structure of α-Fe_2O_3. In a brief procedure, the α-Fe_2O_3 powder sample was dispersed in ethanol solution by ultrasonic agitation for a few moments. A drop of the dispersant-solution sample was released on carbon-enhanced copper grids and dried at 80 °C in air.

RESULTS AND DISCUSSION

At the beginning, the α-Fe_2O_3 phase forming mechanism can be explained as follows.[29]

$$[Fe(CN)_6]^{3-} \leftrightarrow Fe^{3+} \rightarrow FeOOH/Fe(OH)_3 \rightarrow \alpha\text{-}Fe_2O_3$$

Under hydrothermal conditions, $[Fe(CN)_6]^{3-}$ ions are dissociated slowly into $Fe^{3+}$and CN^- ions. These Fe^{3+} ions are subsequently hydrolyzed in aqueous solution to produce FeOOH or $Fe(OH)_3$ and then dehydrated to α-Fe_2O_3.

The chemical composition and crystal structure of the THB nanoparticle sample were characterized by the X-ray powder diffraction method. From Figure 1, the X-ray diffraction (XRD)

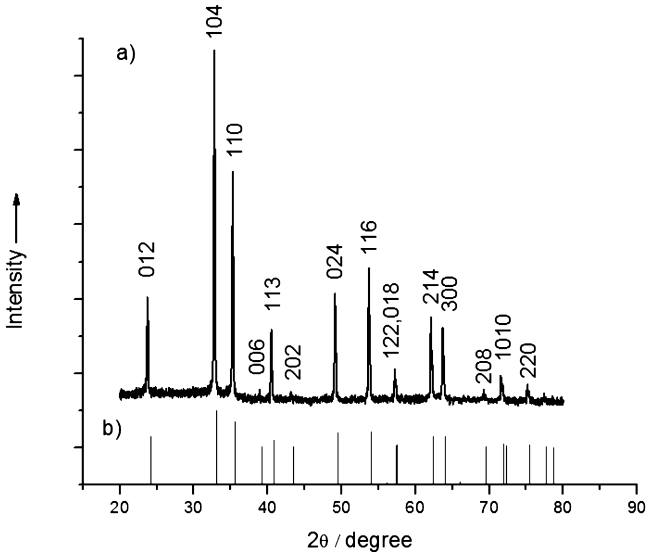

Figure 1. XRD patterns of (a) truncated hexagonal bipyramid iron oxide nanocrytals and (b) hematite, PDF 33-0664.

pattern shows that the THB nanoparticle product is indexed to hexagonal iron oxide structure with cell constants $a = b$ = 0.50356 nm and c = 1.37489 nm, which are consistent with the values in the literature (JCPDS 33-0664). The strong and narrow sharp diffraction peaks are evidence that the as-synthesized product was well crystallized. No other diffraction peaks for impurities were observed.

Representative scanning electron microscope (SEM) images of the THB α-Fe_2O_3 nanoparticle products can be visualized in Figure 2. As shown in Figure 2a, a typical large-area SEM image of the product sample indicates that the as-synthesized α-Fe_2O_3 particles exhibit high uniformity and nanocrystals of well-defined shape. Figure 2b,c in higher magnification SEM images show more clearly the shape of the as-synthesized products. The as-prepared particle product possesses a shape of truncated hexagonal bipyramid as the schematic geometrical model presented in the inset of Figure 2c and in Figure 3a. The THB particle is bound by 12 highly symmetric side-trapezoidal facets corresponding to the probably Miller indices (101), (011), (1$\bar{1}$1), ($\bar{1}$01), ($\bar{1}$11), and (0$\bar{1}$1) and (10$\bar{1}$), (01$\bar{1}$), (1$\bar{1}\bar{1}$),

dx.doi.org/10.1021/cg201252v | Cryst. Growth Des. 2012, 12, 862–868

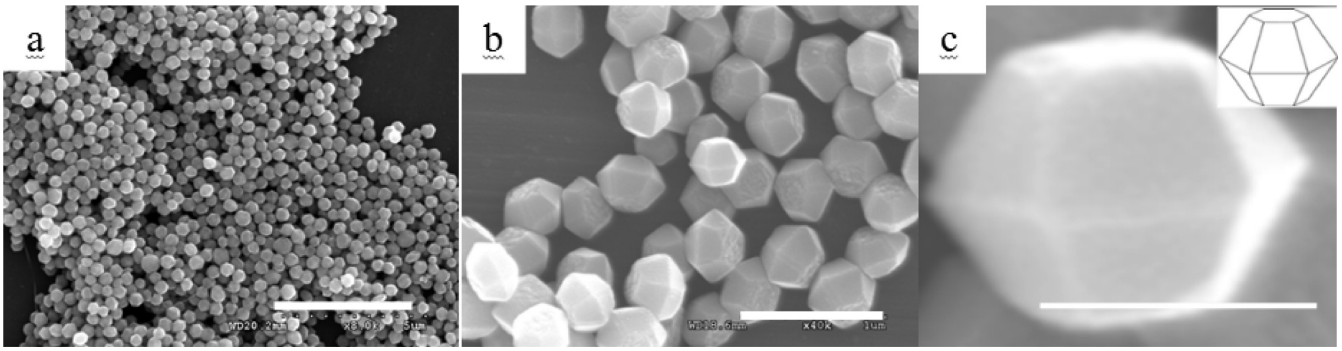

Figure 2. Scanning electron microscopy images of the truncated hexagonal bipyramid α-Fe_2O_3 single-crystalline nanoparticles shown in scale bars (a) 5 μm, (b) 1 μm, and (c) 300 nm.

$(\bar{1}0\bar{1})$, $(\bar{1}1\bar{1})$, and $(0\bar{1}\bar{1})$ and two facets at top and bottom that could be indexed as (001) and $(00\bar{1})$, respectively.

To provide further insight into the nanocrystal structure of these particles, a transmission electron microscopy (TEM) investigation accompanied by high-resolution TEM (HRTEM) and its corresponding selected area electron diffraction (SAED) pattern was also carried out in detail. Figure 3b,c displays the representative TEM images of the as-synthesized α-Fe_2O_3 particles with the truncated hexagonal bipyramid-liked shape and particle size ca. 400 nm. A typical HRTEM image (Figure 3d) was taken at a corner position A of a single THB particle (presented in Figure 3c). The clear lattice fringe image indicates the high crystallinity and single-crystalline nature of the THB α-Fe_2O_3 nanoparticles. Three classes of lattice fringes are resolved, and their corresponding interplane spaces of 0.416, 0.416 and 0.270 nm could be indexed to the interplane distances of the (101), $(10\bar{1})$ and (104) planes, respectively. The SAED pattern taken from an individual single THB α-Fe_2O_3 nanoparticle is shown in the Figure 3e. The diffraction spots are projected by the (101), (006), (104), and (113) planes and their equivalent planes under an incident electron beam. This result clearly suggests that the structures of as-synthesized THB α-Fe_2O_3 nanoparticles are single crystals. In addition, the analysis of chemical composition of these THB nanoparticles was further confirmed by the energy-dispersive X-ray spectroscopy (EDS) method as presented in the Figure 3f, in which the signals of Cu came from Cu grid substrate and atom ratio of Fe/O is around 38.26:57.82 for the product, which agrees well with the value calculated from the formula of hematite to be of 2:3. On the basis of the above structural information, we can conclude that the as-synthesized α-Fe_2O_3 nanoparticle is a single crystal and bound by 12 side symmetric trapezoidal facets with the crystal Miller indices {101} and two other {001} facets at the tops. This morphology is quite well matched with the ideal geometric model of the THB presented in Figure 3.

One of the most important characteristics of a semiconductor is its band gap energy, E_g. In order to determine this parameter, the optical tool applied to measure is calculating the intercept of the extrapolated linear fit in the experiment data of the Tauc plot, $(F(R)h\nu)^n$ versus incident photon energy $(h\nu)$ near the absorption edge,[30] in which $F(R)$ is the absorption coefficient of the material that was converted from the diffuse reflectance (light scattered to all angles) by the Kubelka–Munk function, $F(R) = (1 - R)^2/(2R)$, where R is reflectance.[31] The value of the exponent n denotes the nature of the material. For the hematite, an indirect band gap material, this value is 2.[30] The optical absorbance and Tauc plots of the THB hematite powder were shown in the Figure 4. The optical properties of the as-synthesized product can be easily visualized; the optical absorption band is from 300 to 600 nm and the indirect band gap is 2.08 eV, which closely matches the value reported in the literature.[32] It was reported that[33] the optical property of hematite changes as a result of change in shape and size. The light-scattering properties of material change with respect to its size and morphology, which lead to changes in the optical properties. The electronic transition occuring in the optical absorption spectra of Fe^{3+}substance includes three types:[34] (1) the Fe^{3+} ligand field transition or the d–d transitions, (2) the ligand–metal charge-transfer transitions, and (3) the pair excitations of two adjacent Fe^{3+} cations that are magnetically coupled. Figure 4a shows that optical absorption of THB hematite nanoparticles occurs in the wavelength region of 300–600 nm, which could be attributed to the electronic transition for the charge localized to the FeO_6 coordination site (e.g., Fe^{3+} ligand field and $O^{2-} \rightarrow Fe^{3+}$ charge-transfer transition) and the adjacent Fe^{3+} cations.[35]

To understand the role of reactants used throughout the synthetic process, as well as the crystal growth mechanism to form this morphology, various experiments were carried out in different reaction conditions. As mentioned above, the THB α-Fe_2O_3 particles were fabricated with the aid of CMC and N_2H_4 molecules. The role of CMC and N_2H_4 molecules used in this route is very important to form uniform THB nanoparticles, which acts as dispersant agents and capping agent. It was reported that[36] the CMC molecule possesses many carboxymethyl side groups, which suppresses CMC backbones from getting close to each other as dispersing in a solution. Thus, when these CMC molecules are dispersed into the reaction solution, they will form numerous "channels" in the reaction system that not only limit the crystal growth leading to the formation of α-Fe_2O_3 nanoparticles with much smaller size but also result in homogeneous particle size distribution. On the other hand, N_2H_4 molecules in the reaction solution act as capping agents by adsorbing onto the crystal planes of the initial α-Fe_2O_3 nuclei lead to decrease of the crystal growth rate along the direction of the adsorbed planes by deactivation. Adsorption occurs, which could originate from an acceptor–donor mechanism between the free electron pairs on N atoms of N_2H_4 molecules and exposed Fe^{3+} cations on the surface of the α-Fe_2O_3 germs. The amount of hydrazine molecules adsorbed onto different planes of a hematite crystal is different because the adsorption is dependent on the density of exposed Fe^{3+} cations on the plane of α-Fe_2O_3 crystal. As a previous work

dx.doi.org/10.1021/cg201252v | Cryst. Growth Des. 2012, 12, 862–868

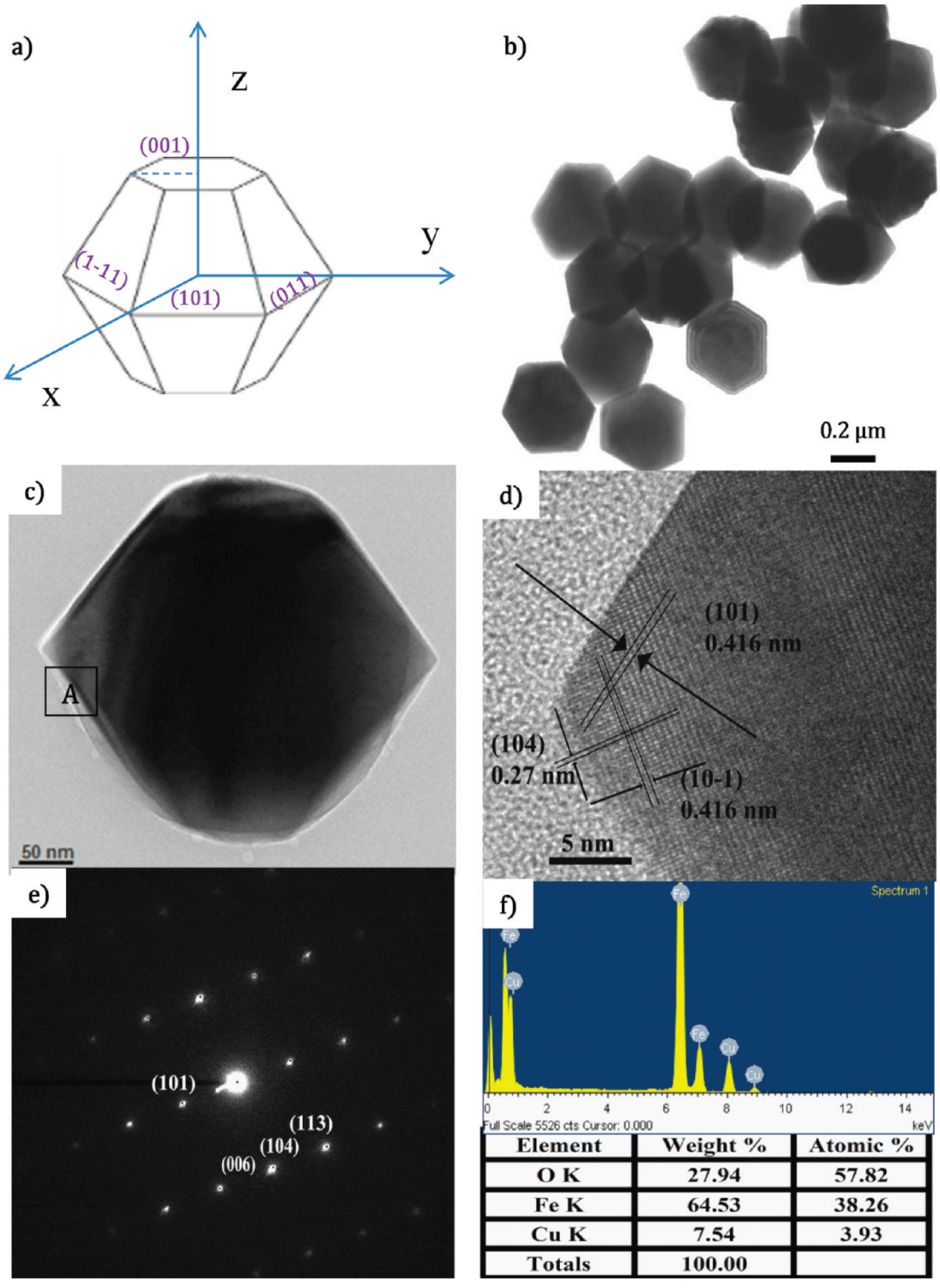

Element	Weight %	Atomic %
O K	27.94	57.82
Fe K	64.53	38.26
Cu K	7.54	3.93
Totals	100.00	

Figure 3. (a) The geometrical model of a truncated hexagonal bipyramid shape bound by {101} and {001} facets, (b, c) TEM images of the truncated hexagonal bipyramid iron oxide nanocrystal, (d) HRTEM image of the truncated hexagonal bipyramid taken at the corner A, (e) SAED pattern of the particle, and (f) EDS spectrum of the sample.

presented,[28] the different densities of exposed Fe^{3+} cations on some low-index planes of a α-Fe_2O_3 crystal is shown in Table 1. From the data in this table, it is obvious that the density of exposed Fe^{3+} cations on the plane (100) is 0.1158 $Å^{-2}$ higher than that on the others. Therefore, the amount of hydrazine molecules adsorbed on this plane, as well as their equivalent planes, is higher compared with that on the other planes. This means that the crystal growth rate along the direction of these planes is lower than that of others. Due to this and on the basis of the hematite crystal structure, the anisotropic growth along six directions of equivalent planes {100} at a low rate and two directions of equivalent planes {001} at a slightly higher rate lead to form the shape of particle as truncated hexagonal bipyramid. This is elucidated by the SEM image of the obtained product presented in Figure 4c. In another experimental situation, when the amount of hydrazine was increased while

dx.doi.org/10.1021/cg201252v | Cryst. Growth Des. 2012, 12, 862–868

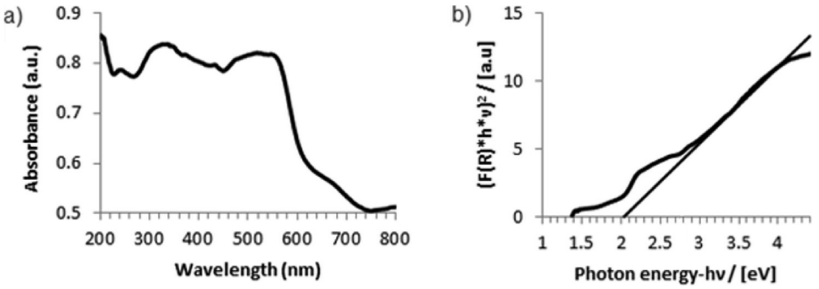

Figure 4. (a) The absorption spectra and (b) the Tauc plot, $(F(R)h\nu)^n$ versus $h\nu$ (n = 2 for the indirect band gap materials) for the THB α-Fe_2O_3 particle powder.

Table 1. The Density of Exposed Fe^{3+} Cations on Some Planes of Hematite Crystal[a]

plane	Fe^{3+}	U [Å]	V [Å]	θ (deg)	S [Å^2]	D [Å^{-2}]
001	2	5.036	5.036	120	21.96	0.0911
012	2	5.035	5.419	90	27.28	0.0733
110	4	7.397	5.419	95.7	39.89	0.100
104	4	7.397	5.035	90	38.75	0.103
100	8	13.720	5.035	90	69.08	0.1158
111	8	8.721	14.642	72.7	121.92	0.0656

[a] U, the length of the cell; V, the width of the cell; θ, the angle between U and V; S, the area of the cell; D, number density of Fe^{3+} cations. Reprinted with permission from ref 28 for interpretation of forming mechanism of the morphologies. Copyright 2010 Wiley.

other reactants were kept constant in the reaction solution, the reaction environment becomes more basic, which accelerates production of new initial nuclei and increases the crystal growth rate. Consequently, the capping role of N_2H_4 molecules is in part ineffective and leads to the crystalline planes with high density of exposed Fe^{3+} cations for growing more strongly and producing inhomogeneous morphologies of product in a majority of octahedral-like (the inset of Figure 5d), oblique cubic (the inset of Figure 5e), and unidentified shapes. The as-obtained Fe_2O_3 morphologies are presented in Figure 5d,e,f with the reaction conditions as shown in the caption of Figure 5. Furthermore, taking into account the role of the $Fe(CN)_6^{3-}$ complex used as a precursor in this synthetic method, $K_3[Fe(CN)_6]$ salt plays an important role in the formation of this morphology. As reported by Wang and co-workers,[23] the $Fe(CN)_6^{3-}$ complexed ion is very stable in aqueous solution at ambient conditions ($K_s = 1.0 \times 10^{42}$) and weakly dissociated in hydrothermal conditions. Therefore, the uniformity of the product might be also attributed to the contribution of slowly produced Fe^{3+} ions from weak dissociation of the $Fe(CN)_6^{3-}$ under hydrothermal conditions, which could be moderate for the crystal growth process in regularity. In another experiment, an aqueous solution of $K_3[Fe(CN)_6]$, 0.02 M, in the absence of CMC and N_2H_4 was treated by hydrothermal route at 160 °C for 8 h, and micropine dendritic morphology was obtained (as shown in the Figure 5a. The weak dissociation of $Fe(CN)_6^{3-}$ ions and the crystal growth along six equivalent directions of the hematite crystal structure result in this morphology. This result is similar to the previous reports in the literature.[23,37] Meanwhile, with the presence of CMC molecules at the concentration of 3.5 g/L in the reaction solution of

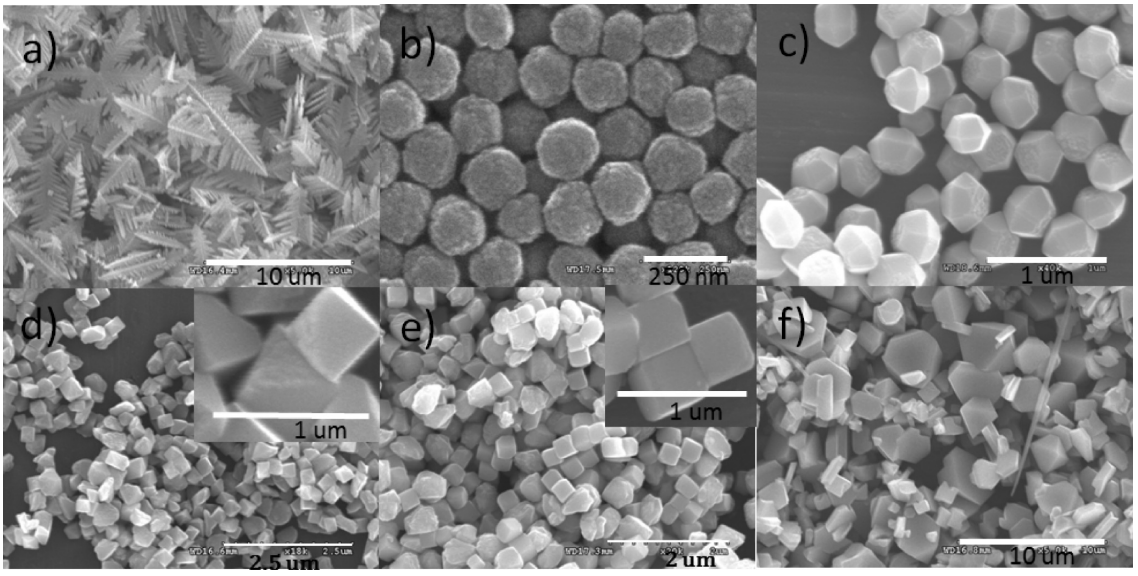

Figure 5. Morphologies of the final α-Fe_2O_3 product obtained with various reactants under hydrothermal reaction conditions at 160 °C for 8 h: (a) $K_3[Fe(CN)_6]$, 0.02 M, in the absence of CMC and N_2H_4, (b) $K_3[Fe(CN)_6]$, 0.02 M, in the presence of CMC, 3.5 g L^{-1}, (c) $K_3[Fe(CN)_6]$, 0.02 M, with the addition of CMC, 3.5 g L^{-1}, and N_2H_4, 1.5 wt %, (d) $K_3[Fe(CN)_6]$, 0.02 M, with the addition of CMC, 3.5 g L^{-1}, and N_2H_4, 4.5 wt %, (e) $K_3[Fe(CN)_6]$, 0.02 M, with the addition of CMC, 3.5 g L^{-1}, and N_2H_4, 6.0 wt %, and (f) $K_3[Fe(CN)_6]$, 0.02 M, with the addition of CMC, 3.5 g L^{-1}, and N_2H_4, 8.0 wt %.

dx.doi.org/10.1021/cg201252v | Cryst. Growth Des. 2012, 12, 862–868

$K_3[Fe(CN)_6]$, 0.02 M, through hydrothermal treatment process, the spherical form was produced (presented in Figure 5b) with a diameter of around 200 nm. These results provided evidence that the isotropic growth of initial α-Fe_2O_3 nuclei and confinement by "channel" of CMC molecules, the subsequent Ostwald ripening process resulted in the aggregated hematite spheres. The XRD patterns shown in the Figure 6 confirmed

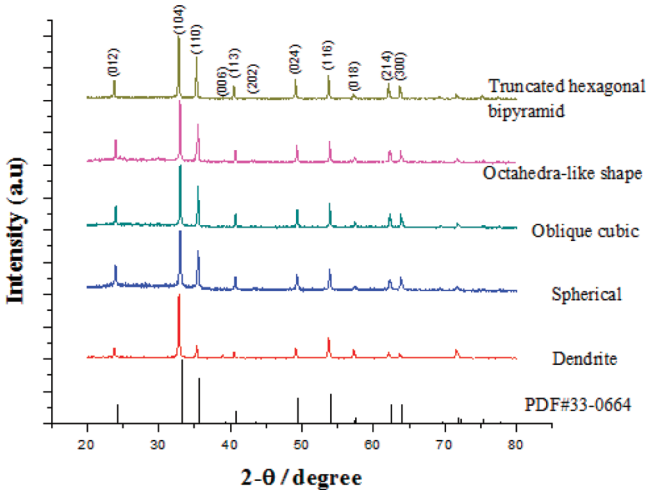

Figure 6. XRD patterns of the as-synthesized hematite morphologies.

that these morphologies are hematite phases without any impurity.

Based on the above discussions, a possible formation mechanism of the hematite morphologies is proposed as the schematic illustration in Figure 7. The aqueous solution of

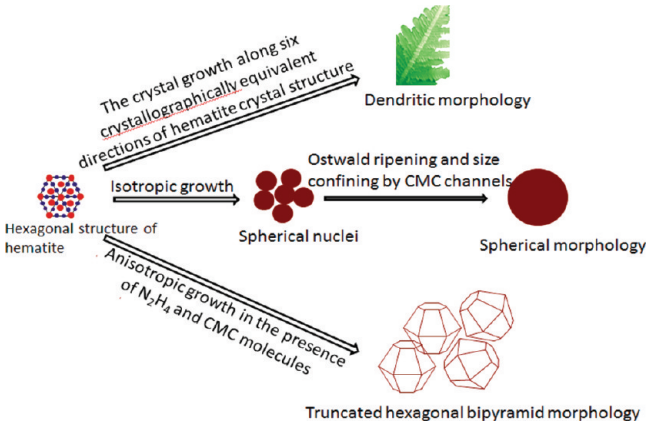

Figure 7. Schematic illustration for formation process of the hematite morphologies.

$K_3[Fe(CN)_6]$ precursor was treated under hydrothermal conditions. First, without the addition of CMC and N_2H_4 molecules, the crystal growth along six crystallographically equivalent directions of the hematite crystalline structure resulted in the dendritic shape. Second, with the addition of CMC molecules in the reaction solution, the isotropic growth of the hematite crystalline structure in the bounds of "CMC channels" and the subsequent Ostwald ripening process generated spherically aggregated α-Fe_2O_3 particles. Third, with the addition of CMC and N_2H_4 molecules in the reaction solution at a suitable concentration, the anisotropic growth along six equivalent directions of planes {100} at a slow rate and two other equivalent directions of planes {001} at a faster rate resulted in the THB shape.

The magnetic behavior of the THB α-Fe_2O_3 nanoparticles was also investigated. Hematite is antiferromagnetic. Rhombohedral crystalline bulk α-Fe_2O_3 possesses a weak ferromagnetic property above the Morin transition temperature $T_M \simeq 260$ K at which the magnetic phase transition from the canted ferromagnetic phase to another antiferromagnetically ordered state.[38] This material also has a high Néel transition temperature $T_N \simeq 960$ K.[39] The curves of temperature dependence (60−300 K) of the zero-field-cooled (ZFC) and field-cooled (FC) magnetization under 100 Oe for the THB α-Fe_2O_3 nanoparticles are shown in Figure 8a. The determined T_M value is about 227 K lower than that of bulk hematite. The curve also shows another decreasing point in magnetization at the temperature of approximately 119 K. This phenomenon might be related to the difference in the size of the particle[40] and magnetic sensitivity to the morphology.[41] Correspondingly, the hysteresis loops shown in Figure 8b indicate the coercivity forces of 328 Oe at 300 K and 288 Oe at 60 K. It can be also seen that the saturation point does not reach up to the maximum applied magnetic field. These results revealed that below the Morin temperature, the sample still shows weak ferromagnetism, which means that a long-range magnetic property still remains at low temperature. The recent studies show that the magnetic property of hematite is influenced by numerous factors including surface behaviors (e.g., absorbed ion species, exposed facets, etc.), size distribution, morphology, crystal structure and so on of material.[28,42−44] Taking into account one of these factors presented above is morphology of this contribution. The morphology of THB hematite crystalline nanoparticles exposes facets {101} and {001}, which have high surface energy of 1.36 and 1.145 J m^{-2}, respectively,[45] and may show defect-controlled ferromagnetism because of the structure sensitivity of defect ferromagnetism.[42] Moreover, the THB hematite nanoparticle shape is highly symmetric, which may be attributed to the shape anisotropy that holds them back from magnetizing along directions other than their easy magnetic axis.[46] Obviously, further works should be done to understand better the factors influencing the magnetic properties of this material.

CONCLUSIONS

A new morphology with THB nanoparticle shape of α-Fe_2O_3 material was found by a simple hydrothermal synthetic route. The as-synthesized THB nanoparticles are single crystals that are bound by 12 same-side crystalline facets {101} and two other same facets {001} at the tops. High uniformity of the THB hematite particles was exhibited, and the particle size is ca. 400 nm. The chemical composition and crystalline structure indicate that this iron oxide is a pure hematite phase. The experimental investigations provided insight on the role of the reactants used in the synthetic process and a diagram schematically illustrating formation of this morphology was also proposed. The study on optical and magnetic properties of the THB single-crystalline hematite nanoparticles shows great interests and would be a class of promising functional material for many applications. However, extensive experiments should be performed on this α-Fe_2O_3 structure to understand better its other properties for practical applications.

dx.doi.org/10.1021/cg201252v | Cryst. Growth Des. 2012, 12, 862−868

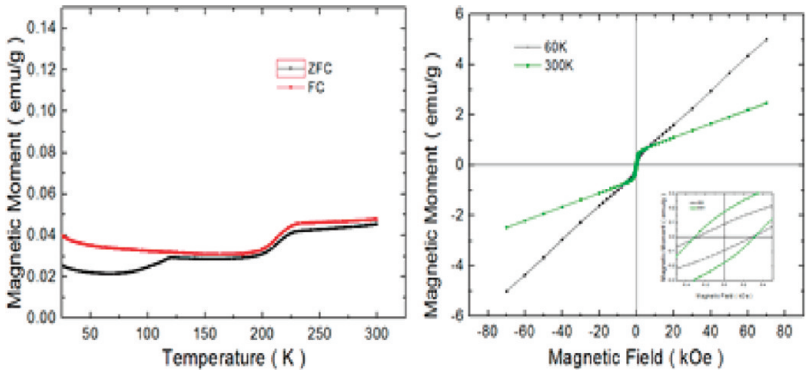

Figure 8. The magnetization vs temperature FC/ZFC curves (left) under 100 Oe of the truncated hexagonal bipyramid particles and the magnetic hysteresis loop (right) of the truncated hexagonal bipyramid particles at 60 and 300 K.

AUTHOR INFORMATION

Corresponding Author

*E-mail: yskang@sogang.ac.kr.

ACKNOWLEDGMENTS

This work was supported by The Korea Center for Artificial Photosynthesis (KCAP) located in Sogang University funded by the Ministry of Education, Science, and Technology (MEST) through the National Research Foundation of Korea (Grant NRF-2009-C1AAA001-2009-0093879).

REFERENCES

(1) Suryanarayana, C. *Non-Equilibrium Processing of Materials*; Pergamon Materials Series; Pergamon Press: New York.

(2) Mohapatra, S. K.; John, S. E.; Banerjee, S.; Misra, M. *Chem. Mater.* **2009**, *21*, 3048−3055.

(3) Brillet, J.; Gratzel, M.; Sivula, K. *Nano Lett.* **2010**, *10*, 4155−4160.

(4) Ling, Y.; Wang, G.; Wheeler, D. A.; Zhang, J. Z.; Li, Y. *Nano Lett.* **2011**, *11*, 2119−2125.

(5) Cesar, I.; Kay, A.; Martinez, J. A. G.; Gratzel, M. *J. Am. Chem. Soc.* **2006**, *128*, 4582−4583.

(6) Kay, A.; Cesar, I.; Gratzel, M. *J. Am. Chem. Soc.* **2006**, *128*, 15714−15721.

(7) Huo, L.; Li, W.; Lu, L.; Cui, H.; Xi, S.; Wang, J.; Zhao, B.; Shen, Y.; Lu, Z. *Chem. Mater.* **2000**, *12*, 790−794.

(8) Sivula, K.; Zboril, R.; Formal, F. L.; Robert, R.; Weidenkaff, A.; Tucek, J.; Frydrych, J.; Gratzel, M. *J. Am. Chem. Soc.* **2010**, *132*, 7436−7444.

(9) Cherepy, N. J.; Liston, D. B.; Liston, D. B.; Lovejoy, J. A.; Deng, H.; Zhang, J. Z. *J. Phys. Chem. B* **1998**, *102*, 770−776.

(10) Hu, X.; Yu, J. C.; Gong, J.; Li, Q.; Li, G. *Adv. Mater.* **2007**, *19*, 2324−2329.

(11) Tsodikov, M. V.; Rostovshchikova, T. N.; Smirnov, V. V.; Kiseleva, O. I.; Maksimov, Y. V.; Suzdalev, I. P.; Ikorskii, V. N. *Catal. Today* **2005**, *105*, 634−640.

(12) Zhang, L.; Wang, Y.; Ji, H.; Wei, Y.; Wu, N.; Zuo, B.; Wang, Q. *J. Catal.* **2005**, *229*, 114−118.

(13) Jiao, F.; Harrison, A.; Jumas, J. C.; Chadwick, A. V.; Kockelmann, W.; Bruce, P. G. *J. Am. Chem. Soc.* **2006**, *128*, 5468−5474.

(14) Yu, R.; Li, Z.; Wang, D.; Lai, X.; Xing, C.; Yang, M.; Xing, X. *Scr. Mater.* **2010**, *63*, 155−158.

(15) Yu, R.; Li, Z.; Wang, D.; Lai, X.; Xing, C.; Xing, X. *Solid State Science* **2009**, *11*, 2056−2059.

(16) Li, Z.; Lai, X.; Wang, H.; Mao, D.; Xing, C.; Wang, D. *Nanotechnology* **2009**, *20*, 245603.

(17) Mao, D.; Yao, J.; Lai, X.; Yang, M.; Du, J.; Wang, D. *Small* **2011**, *7*, 578−582.

(18) Suber, L.; Fiorani, D.; Imperatori, P.; Foglia, S.; Montone, A.; Zysler, R. *Nanostruct. Mater.* **1999**, *11*, 797−803.

(19) Wang, S. B.; Min, Y. L.; Yu, S. H. *J. Phys. Chem. C* **2007**, *111*, 355−3554.

(20) Jia, C. J.; Sun, L. D.; Yan, Z. G.; Pang, Y. C.; You, L. P.; Yan, C. H. *J. Phys. Chem. C* **2007**, *111*, 13022−13027.

(21) Li, L.; Chu, Y.; Liu, Y.; Dong, L. *J. Phys. Chem. C* **2007**, *111*, 2123−2127.

(22) Ngo, A. T.; Pileni, M. P. *J. Appl. Phys.* **2002**, *92*, 4649.

(23) Cao, M.; Liu, T.; Sun, G.; Wu, X.; Hu, C.; Wang, Z. L. *Angew. Chem., Int. Ed.* **2005**, *44*, 4197−4201.

(24) Zhu, L. P.; Xiao, H. M.; Liuab, X. M.; Fu, S. Y. *J. Mater. Chem.* **2006**, *16*, 1794−1797.

(25) Lv, B.; Xu, Y.; Wua, D.; Sun, Y. *Chem. Commun.* **2011**, *47*, 967−969.

(26) Matijevie, E. *Chem. Mater.* **1993**, *5*, 412−426.

(27) Domingo, C.; Clemente, R. R.; Blesa, M. *J. Colloid Interface Sci.* **1994**, *165*, 244−252.

(28) Lv, B.; Liu, Z.; Tian, H.; Xu, Y.; Wu, D.; Sun, Y. *Adv. Funct. Mater.* **2010**, *20*, 3987−3996.

(29) Zhang, X.; Sui, C.; Gong, J.; Su, Z.; Qu, L. *J. Phys. Chem. C* **2007**, *111*, 9049−9054.

(30) Misho, R. H.; Murad, W. A. *Sol. Energy Mater. Sol. Cells* **1992**, *27*, 335−345.

(31) Kubelka, P.; Munk, F. Z. *Tech. Phys. (Leipzig)* **1931**, *12*, 593.

(32) Veyssieres, L.; Sathe, C.; Butorin, S. M.; Shuh, D. K.; Nordgren, J.; Guo, J. *Adv. Mater.* **2005**, *17*, 2320−2323.

(33) Lian, J.; Duan, X.; Ma, J.; Peng, P.; Kim, T.; Zheng, W. *ACS Nano* **2009**, *3*, 3749−3761.

(34) He, Y. P.; Miao, Y. M.; Li, C. R.; Wang, S. Q.; Cao, L.; Xie, S. S.; Yang, G. Z.; Zou, B. S. *Phys. Rev. B* **2005**, *71*, No. 125411.

(35) Sherman, D. M. *Am. Mineral.* **1985**, *70*, 1262−1269.

(36) http://class.fst.ohio-state.edu/fst621/Additive%20classes/cmctlk.pdf

(37) He, K.; Xu, C. Y.; Zhen, L.; Shao, W. Z. *Mater. Lett.* **2008**, *62*, 739−742.

(38) Morin, F. *J. Phys. Rev.* **1950**, *78*, 819.

(39) Gronvold, F. *J. Phys. Chem. Solids.* **1975**, *36*, 249−256.

(40) Zysler, R. D. *Phys. Rev. B* **2003**, *68*, No. 212408.

(41) Sorescu, M. *J. Appl. Phys.* **1999**, *85*, 5546.

(42) Yin, J.; Yu, Z.; Gao, F.; Wang, J.; Pang, H.; Lu, Q. *Angew. Chem., Int. Ed.* **2010**, *49*, 6328−6332.

(43) Salazar-Alvarez, G.; Qui, J.; Sepelak, V.; Bergmann, I.; Vasilakaki, M.; Trohidou, K. N.; Ardisson, J. D.; Macedo, Q. A. A.; Mikhaylova, M.; Muhammed, M.; Baro, M. D.; Nogues, J. *J. Am. Chem. Soc.* **2008**, *130*, 13234−13239.

(44) Liu, L.; Kou, H. Z.; Mo, W.; Liu, H.; Wang, Y. *J. Phys. Chem. B* **2006**, *110*, 15218−15223.

(45) Guo, H.; Barnard, A. S. *J. Mater. Chem.* **2011**, 11566.

(46) Wang, J.; Chen, Q.; Zeng, C.; Hou, B. *Adv. Mater.* **2004**, *16*, 137.